Hydrodynamic Fluctuations in Confined Particle-Laden Fluids

Nicolas Desreumaux,[1] Jean-Baptiste Caussin,[2,1] Raphael Jeanneret,[1] Eric Lauga,[3,4] and Denis Bartolo[2,1]

[1]*Laboratoire de Physique et Mécanique des Milieux Hétérogènes, PMMH, ESPCI ParisTech, CNRS UMR 7636, Université Paris 6, and Université Paris 7, 10 Rue Vauquelin, 75005 Paris, France*

[2]*Laboratoire de Physique de l'Ecole Normale Supérieure de Lyon, Université de Lyon, and CNRS, 46, Allée d'Italie, F-69007 Lyon, France*

[3]*Department of Mechanical and Aerospace Engineering, University of California San Diego, 9500 Gilman Drive, La Jolla California 92093-0411, USA*

[4]*Department of Applied Mathematics and Theoretical Physics, Centre for Mathematical Sciences, University of Cambridge, Wilberforce Road, Cambridge CB3 0WA, United Kingdom*

(Received 15 April 2013; published 10 September 2013)

We address the collective dynamics of non-Brownian particles cruising in a confined microfluidic geometry and provide a comprehensive characterization of their spatiotemporal density fluctuations. We show that density excitations freely propagate at all scales, and in all directions even though the particles are neither affected by potential forces nor by inertia. We introduce a kinetic theory which quantitatively accounts for our experimental findings, demonstrating that the fluctuation spectrum of this nonequilibrium system is shaped by the combination of truly long-range hydrodynamic interactions and local collisions. We also demonstrate that the free propagation of density waves is a generic phenomenon which should be observed in a much broader range of hydrodynamic systems.

DOI: 10.1103/PhysRevLett.111.118301 PACS numbers: 82.70.Kj, 47.57.−s, 47.61.−k

Understanding the collective dynamics of non-Brownian particles in viscous fluids is a long-standing challenge in fluid mechanics. For example, many features of sedimentation in a quiescent fluid are still poorly understood. Rather than falling along straight lines, as an isolated particle does, sedimenting particles experience swirling motion correlated over large finite distance, the physical origin of which has been under debate for more than 30 years [1,2]. The conceptual complexity of this collective dynamics contrasts with the formal simplicity of the (linear) Stokes equation that rules low-Reynolds-number flows. Immersed bodies generically affect both the momentum and the mass transfers of the fluid, even when not driven by external fields. As a result, long-range interactions arise between the particles due to the interplay between the local velocity of the fluid and the motion of the particles. They vanish only for uniform flows, for which the particles would be all advected at the same speed as the fluid, irrespective of their spatial distribution. Such a condition is never achieved when the fluid is confined by rigid walls or obstacles. Friction with the bounding walls causes strong distortions of the flow field, inducing effective interactions between the particles [3–6]. As it turns out, the transport of particle-laden fluid through rigidly confined geometries is involved in a number of industrial and natural processes, including filtration [7], colloid deposition on solid surfaces [8,9], droplet-based microfluidics [10,11], blood microflows [12], protein motion in lipid membranes [3], and bacteria swarming [13,14]. Understanding the particle transport in confined films is a necessary first step toward the description of particle traffic in more complex geometries such as ordered, or random porous networks. Recently, pioneering experiments probed the propagation of density heterogeneities in bidimensional emulsions and droplet streams [15,16]. Focusing on a semi-local quantity, the droplet density averaged over the channel width, Beatus *et al.* revealed the propagation of longitudinal nonlinear density waves, Burgers shocks, resulting from the linear variation of the droplet speed with the local density [15]. However, this observation does not account for the complexity of the structural [17], and spatiotemporal fluctuations observed at all scales in rigidly confined particle-laden fluids, regardless of their specific geometry, composition, and driving mechanism [13,15,17–19].

Here, we combine advanced microfluidic experiments and kinetic theory to shed light on the collective dynamics of particles advected in shallow microchannels. We first characterize their density fluctuations. We show that they freely propagate, at all scales and in all directions, in a dispersive manner. We then quantitatively demonstrate how the interplay of hydrodynamic and steric interactions shape the fluctuation spectrum of the linear density waves. Finally, we close this Letter by stressing that the impact of our results goes beyond microfluidic systems. We show how to use bidimensional microfluidic emulsions as a proxy to probe collective effects in a much broader range of hydrodynamic systems including diffusiophoretic suspensions, foams, or emulsions, cruising through porous media, and confined sedimentation.

We developed a model microfluidic experiment which made it possible to track the individual positions of hundreds of thousands of identical droplets interacting hydrodynamically in a shallow channel. Briefly, the system consists of a monodisperse oil-in-water emulsion flowing

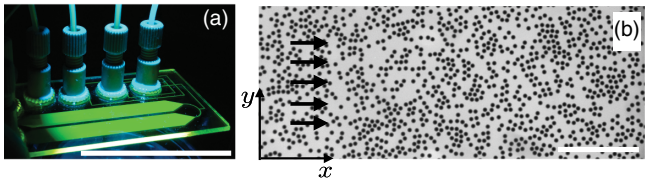

FIG. 1 (color online). (a) Picture of the microfluidic setup. During the experiments one of these two 5-cm-long channels was continuously fed with monodisperse droplets. Scale bar: 5 cm. (b) Typical snapshot of an experimental movie. The black arrows indicate the direction of the flow. Scale bar: 500 μm.

in a shallow microchannel. The length and width of the channel, $L \times W = 5$ cm $\times$ 5 mm, are much larger than its height, $h = 27 \pm 0.1$ μm, which compares with the droplet diameter, see Fig. 1. The emulsion is, therefore, confined in a quasi-2D geometry. The droplets are formed at a conventional flow-focusing junction followed by a dilution module. The fluid flow rates are imposed by high-precision syringe pumps. Etched-glass microchips ensure that the channel dimensions are unaffected by the flow conditions. In addition, the geometry of the junction, and the range of flow rates, are chosen so that the formation of the droplet is unaffected by the dilution flow. Therefore, we accurately controlled both the droplet radius, R_d, and the average area fraction, ϕ, occupied by the emulsion. Here, we report results obtained for $R_d = 16.7 \pm 0.3$ μm ($R_d/h = 0.62$), and $0.21 < \phi < 0.56$. Varying the droplet sizes up to $R_d \sim 2h$ does not qualitatively change our measurements. The droplets are visualized using fluorescence imaging. For each experiment we tracked $\sim 10^5$ particle trajectories in a region close to the center of the main channel, Fig. 1(b). For more details, see the Supplemental Material [20].

Without droplets, the fluid flow would be uniform along the x direction in the observation region. This is evidenced by the linear trajectories followed by isolated droplets cruising along the channel. Conversely, even at the smallest surface fraction, the droplets undergo large fluctuations in their motion, as shown in the movie in the Supplemental Material [21]. These fluctuations lead to the formation of particle clusters at all scales. These clusters are clearly seen to travel at a speed that is different from the mean droplet velocity. Density bands transverse to the flow are faster than the longitudinal ones. However, these clusters are transient structures, they form and break apart in a continuous fashion. Our purpose is to elucidate the physical mechanisms responsible for this complex and fluctuating dynamics. To quantify the spatiotemporal fluctuations of the droplet density field $\rho(\mathbf{r}, t)$, where $\mathbf{r} = (x, y)$, we measure its power spectrum. Introducing the Fourier transform of the local density, $\rho_{\mathbf{q},\omega'} = (1/2\pi) \times \int \rho(\mathbf{r}, t) e^{i(\mathbf{q}\cdot\mathbf{r} - \omega' t)} d\mathbf{r} dt$, the power spectrum is defined as $|\tilde{\rho}_{\mathbf{q},\omega'}|^2$, where $\tilde{\rho}(\mathbf{r}, t) \equiv \rho(\mathbf{r}, t) - \langle \rho(\mathbf{r}, t) \rangle$. Practically, ρ is computed from the particle positions as $\rho(\mathbf{r}, t) \equiv \sum_i \mathcal{G}(\mathbf{r} - \mathbf{r}_i(t))$, where $\mathbf{r}_i(t)$ is the position of the ith droplet, and where $\mathcal{G}$ is a Gaussian shape function.

In Fig. 2(a), we show a cut of a typical power spectrum in the (ω', q_x) plane. This example corresponds to $\phi = 0.39$, and to $q_y R_d = 0.2$. Several important comments are in order. (i) The power spectrum is localized in the Fourier space, which is the hallmark of propagative dynamics for the density fluctuations, as first noted in Ref. [15] for the specific case of the y-averaged density mode ($q_y = 0$). We stress that compression modes propagate even though the droplets do not interact via potential forces, and even though their inertia is negligible compared to the viscous friction at this scale. These "sound" modes originate only from the hydrodynamic coupling between the advected particles. (ii) The curve on which the spectrum is peaked corresponds to the dispersion curve of the density waves. It deviates markedly from a straight line at moderate wavelengths. The hydrodynamic interactions do not merely

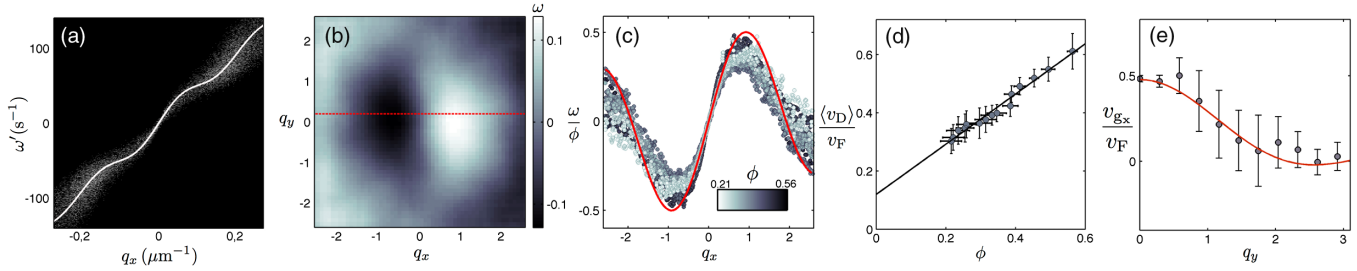

FIG. 2 (color online). (a) Gray-scale power spectrum of the density fluctuations plotted in the (q_x, ω') plane for $q_y = 0.2/R_d$, $\phi = 0.39$, and $v_F = 1$ mm/s. Solid line: theoretical prediction for the location of the dispersion curve. (b) Experimental dispersion curve $\omega(q_x, q_y)$, $\phi = 0.39$. Recall that units are chosen so that $R_d = 1$, and $v_F = 1$. Given the size of the observation window, the smallest finite value for q is given by $qW = 11.6$. The dotted line indicates the q_y value corresponding to the power spectrum shown in (a). (c) Renormalized dispersion relations in the moving frame, $q_y = 0$. Circles: experimental data. Solid line: theoretical prediction, Eq. (6), with no adjustable parameter. (d) Variations of the mean droplet velocity with ϕ. Circles: experimental data. Solid line: best linear fit. The error bars account for statistical fluctuations, and correspond to the standard deviation. (e) v_{g_x} plotted versus q_y at $q_x = 0$. Circles: experimental data for $\phi = 0.56$. Solid line: theoretical prediction with no adjustable parameter deduced from Eq. (6). The error bars correspond to a 95% confidence interval in the measurement of v_{g_x} from the slope of the dispersion curve.

renormalize the mean advection speed but cause the density fluctuations to propagate in a dispersive fashion. (iii) The global shape of the spectrum is conserved for every area fraction, and more surprisingly for every wave vector q_y provided that the wavelength remains larger than the particle size (see below).

In all that follows, we discard the trivial nondispersive contribution due to the advection at the mean droplet velocity $\langle \mathbf{v}_d \rangle$. We focus on the density fluctuations in the frame moving at $\langle \mathbf{v}_d \rangle$, and introduce the reduced pulsation $\omega \equiv \omega' - \langle v_d \rangle q_x$. Experiments done at different area fractions, and thus at different continuous phase velocities due to dilution, are compared by normalizing the wave vectors by R_d^{-1}, and the pulsations by v_F/R_d, where v_F is the velocity of the continuous phase imposed by the syringe pumps. Figure 2(b) shows a typical dispersion relation: $\omega = \omega(q_x, q_y)$, obtained for $\phi = 0.39$. The spectrum is symmetric along the q_y direction as expected from the symmetry of the system. Furthermore, density fluctuations propagate in all directions except in the one strictly transverse to the flow ($q_x = 0$). In addition, the dispersion curve displays an axial symmetry with respect to the q_y axis. It is worth noting that the sign of the associated phase velocity changes as q_x increases. The long wavelength excitations propagate downstream, while the short wavelength excitations propagate upstream.

In Fig. 2(c), we show that once renormalized by ϕ, the dispersion relations corresponding to 12 different area fractions collapse on a single master curve. This noticeable collapse is not specific to the purely longitudinal waves and occurs for all the possible q_y values. Our systematic rescaling demonstrates that a unique set of physical mechanisms dictates the collective motion of the droplets, at all scales, regardless of the droplet density.

We now propose a theoretical model which quantitatively accounts for our experimental findings. The instantaneous configuration of the emulsion is fully determined by the positions of N identical axisymmetric particles: $\mathbf{r}_i(t)$, $i = 1 \ldots N$. The dynamics of an isolated particle has proven to be correctly captured by a constant mobility coefficient, μ, defined as $\dot{\mathbf{r}}_i(t) \equiv \mu \mathbf{v}(\mathbf{r}_i, t)$ where $\mathbf{v}(\mathbf{r}, t)$ is the in-plane fluid velocity field averaged over the channel height in the absence of the particle i [15,16]. In our quasi-2D geometry, the fluid flow is potential and derives from the local pressure field, $\mathbf{v} = -G\nabla P$, where $G = h^2/12\eta$, η being the viscosity of the aqueous phase; $\mathbf{v}(\mathbf{r}, t)$ is then fully determined when considering the incompressibility condition, and the no-flux boundary conditions through the sidewalls of the channel. In a particle-free channel, the velocity field would be uniform, $\mathbf{v} = v_F \hat{\mathbf{x}}$. The particles are not passive tracers ($\mu < 1$); therefore, their relative motion with respect to the fluid results in a dipolar disturbance of the surrounding flow [3,4]. The potential dipolar perturbation, $\mathbf{v}^{\mathrm{dip}}(\mathbf{r}, \mathbf{r}_i(t))$, induced at the position $\mathbf{r}$ by a particle located at $\mathbf{r}_i(t)$ is defined by the modified incompressibility relation

$$\nabla \cdot \mathbf{v}^{\mathrm{dip}}(\mathbf{r}, \mathbf{r}_i(t)) = \sigma \partial_x \delta(\mathbf{r} - \mathbf{r}_i(t)), \quad (1)$$

where σ is the dipole strength ($\sigma > 0$). In order to establish the equations of motion of the N particles, we now assume the dipolar disturbances to be pairwise additive. This yields $\dot{\mathbf{r}}_i(t) = \mu v_F \hat{\mathbf{x}} + \mu \sum_{j \neq i} \mathbf{v}^{\mathrm{dip}}(\mathbf{r}_i(t), \mathbf{r}_j(t))$. We now move from these N coupled equations to a hydrodynamic description for the particle density field $\rho(\mathbf{r}, t)$. $\rho(\mathbf{r}, t)$ obeys the conservation equation

$$\partial_t \rho(\mathbf{r}, t) + \nabla \cdot \mathbf{j}(\mathbf{r}, t) = 0. \quad (2)$$

In order to relate the local particle current $\mathbf{j}(\mathbf{r}, \mathbf{t})$ to the local structure of the suspension, we used a conventional kinetic theory framework [22,23]

$$\mathbf{j}(\mathbf{r}, t) = \mu \rho(\mathbf{r}, t) \mathbf{v}_F + \mu \int d\mathbf{r}' \mathbf{v}^{\mathrm{dip}}(\mathbf{r}, \mathbf{r}') \rho^{(2)}(\mathbf{r}, \mathbf{r}', t), \quad (3)$$

where $\rho^{(2)}(\mathbf{r}, \mathbf{r}', t)$ is the two-point distribution function. We now assume that the particle positions decorrelate over a distance as small as one particle diameter. In addition to this mean-field approximation, we also explicitly account for the steric repulsion between the particles via the following closure relation for Eq. (3)

$$\rho^{(2)}(\mathbf{r}, \mathbf{r}') = \begin{cases} 0 & \text{if } |\mathbf{r} - \mathbf{r}'| < 2R_d, \\ \rho(\mathbf{r})\rho(\mathbf{r}') & \text{if } |\mathbf{r} - \mathbf{r}'| \geq 2R_d, \end{cases} \quad (4)$$

where R_d is the radius of a particle. Equations (3) and (4) define the equations of motion for the particle-density field. In principle, the effective extent of the excluded volume could be larger than the particle radius due to short-range intermolecular repulsions and lubrication forces. However, no measurable difference with the actual droplet radius could be observed in our experiments. We now focus on the dynamics of small density fluctuations, $\tilde{\rho}(\mathbf{r}, t)$, around a homogeneous state: $\tilde{\rho}(\mathbf{r}, t) \equiv \rho(\mathbf{r}, t) - \rho_0$, where $\rho_0 = \langle \rho(\mathbf{r}, t) \rangle = \phi/(\pi R_d^2)$. As in our experiments, we work in the frame moving at the mean droplet velocity $\langle \mathbf{v}_d \rangle = \mu v_F \hat{\mathbf{x}} + \mu \rho_0 \int_{|\mathbf{r}-\mathbf{r}'| \geq 2R_d} \mathbf{v}^{\mathrm{dip}}(\mathbf{r}, \mathbf{r}') d\mathbf{r}'$. At leading order in $\tilde{\rho}$, and combining Eq. (3) and (4) ansatz, the current functional that captures both the hydrodynamic interactions (long range) and the contact interactions (short range) remains nonlocal: $\tilde{\mathbf{j}}(\mathbf{r}, t) \equiv \mu \rho_0 \int_{|\mathbf{r}-\mathbf{r}'| \geq 2R_d} \mathbf{v}^{\mathrm{dip}}(\mathbf{r}, \mathbf{r}') \tilde{\rho}(\mathbf{r}', t) d\mathbf{r}'$. However, using Eq. (1) and focusing on particles far from the sidewalls, then $\nabla \cdot \tilde{\mathbf{j}}$ takes a simple local form

$$\nabla \cdot \tilde{\mathbf{j}}(\mathbf{r}, t) = -\frac{\mu \rho_0 \sigma}{4\pi R_d} \int_0^{2\pi} \tilde{\rho}(\mathbf{r} - 2R_d \hat{\mathbf{r}}') \cos\theta' d\theta', \quad (5)$$

where, since $R_d \ll W$, we have used the expression of the dipolar perturbation corresponding to an unbounded domain [4], $\mathbf{v}^{\mathrm{dip}}(\mathbf{r}, \mathbf{r} + 2R_d \hat{\mathbf{r}}') \cdot \hat{\mathbf{r}}' = -(\sigma \cos\theta')/8\pi R_d^2$, with $\hat{\mathbf{r}}' \equiv \cos\theta' \hat{\mathbf{x}} + \sin\theta' \hat{\mathbf{y}}$. We now look for plane wave solutions $\tilde{\rho}(\mathbf{r}, t) = \sum_{\mathbf{q}} \tilde{\rho}_{\mathbf{q}} \exp(i\omega t - i\mathbf{q} \cdot \mathbf{r})$ of Eq. (2). After some

elementary algebra, we infer their dispersion relation, which is our main theoretical result

$$\omega = (\mu\sigma\rho_0)q_x \frac{J_1(2qR_d)}{2qR_d}, \tag{6}$$

where J_1 is the first Bessel function. As ω is real, this relation implies that density waves freely propagate in the channel in qualitative agreement with our experimental observations. It is worth noting that since $\nabla \cdot \tilde{\mathbf{j}}$ is a local quantity, the form of the dispersion relation is generic, and does not depend on the channel size and geometry. In addition, the linear variations of ω with ρ_0 explain the collapse of the normalized dispersion relations on a single master curve over the entire range of wave vectors [Fig. 2(c)].

We now move to a quantitative comparison between our theoretical predictions and our experimental measurements. Equation (6) is fully determined by two physical parameters: the droplet radius R_d, and $\mu\sigma\rho_0$ that quantifies the strength of the hydrodynamic couplings. In order to determine this latter parameter, we exploit another specific feature of the hydrodynamic interactions. Due to their symmetry, the sum of all the dipolar perturbations would leave the mean droplet velocity unchanged in an isotropic and homogeneous system. However, in anisotropic-channel geometries, $\langle \mathbf{v}_d \rangle$ increases linearly with the mean density irrespective of the channel size [11]. At 0th order in $\tilde{\rho}$, $\langle \mathbf{v}_d \rangle = \mu v_F \hat{\mathbf{x}} + (1/2)(\mu\sigma\rho_0)\hat{\mathbf{x}}$. Importantly, this relation provides a direct means to measure independently the last unknown parameter of our theory. The linear increase of the measured value of $\langle v_d \rangle$ with ρ_0 appears clearly in Fig. 2(d). The strength of the hydrodynamic coupling $(\mu\sigma\rho_0)$ can, thus, be inferred from a linear fit [see Fig. 2(d)]. We superimposed our theoretical predictions for the dispersion relation, Eq. (6), both in the laboratory frame and in the frame moving at $\langle \mathbf{v}_d \rangle$ in Figs. 2(a) and 2(c). We find that the agreement between the theory and the experiments is excellent over a wide range of wave vectors and area fractions. Without any free fitting parameters, our model quantitatively captures the dispersive nature of the density fluctuations observed in the flowing emulsions.

To gain additional physical insight into the propagation of the density waves, it is worth looking at the small-q expansion of Eq. (6): $\omega = (1/2)\mu\sigma\rho_0 q_x \times [1 - (1/2)(qR_d)^2] + \mathcal{O}[(qR_d)^4]$. At leading order, this relation is nondispersive (linear) for the wave component parallel to the mean flow. The phase velocity scales linearly with the magnitude of the dipolar coupling σ. In addition, it does not depend explicitly on R_d, which implies that the small-q excitations propagate only due to the long-range hydrodynamic interactions between the particles. Conversely, the dispersive term in $\omega(\mathbf{q})$ explicitly depends on the particle radius. At high q, the propagation of the density waves is set by the combination of the excluded volume interactions and the angular symmetry of the hydrodynamic couplings. To introduce our last quantitative results, we recall that one of the most striking features observed in the flowing emulsions is the propagation of vertical density bands which propagate at a significantly faster speed than the mean droplet flow, see movie in the Supplemental Material [21]. A homogeneous vertical band spanning the entire width of the channel corresponds to the linear superposition of plane waves associated with $q_y = 0$, and with q_x's distributed around $q_x = 0$. In the frame moving at $\langle \mathbf{v}_d \rangle$, their speed is given by the x component of the group velocity $v_{g_x}(q_x, q_y) = \partial\omega/\partial q_x$ evaluated at $q = 0$. In Fig. 2(e), we plot the experimental values of $v_{g_x}(0, q_y)$, which we measured from the slope at the origin of the dispersion curves [as the ones shown in Fig. 2(c)]. Again the agreement with the theoretical curve deduced from Eq. (6) is excellent. This plot reveals that the density bands extended across the entire channel width are the fastest and propagate at velocities 1.5 higher that the mean droplet flow, thereby making them highly visible on the experimental movies.

To close this Letter, we further stress the relevance of our results to a much broader range of physical systems. Two ingredients dictate the collective behavior of the confined emulsions: (i) the hydrodynamic interactions between the particles result from dipolar perturbations to the mean flow, (ii) the particles have a finite size. As it turns out these two features are shared by a number of very distinct hydrodynamic systems. A first class of example concerns the transport of particles in porous media. Regardless of the spatial dimension (2D or 3D), the fluid flow in a porous network is a potential flow at scales larger than the typical pore size. In addition, it has been recently shown that when particles locally obstruct the porous network they induce a dipolar perturbation to the velocity field [18]. Therefore, the dispersive propagation of density excitations is expected to be found in particle filters, blood microvessels, soils, etc. It is also worth noting that the dipolar perturbations to the flow found in Hele-Shaw and in network geometries are not restricted to particles advected by the surrounding fluid. Sedimenting particles, rising bubbles, and even self-propelled particles would move faster than the (confined) host fluid, thereby inducing dipolar perturbations in the far field as well. The same collective phenomenology would be found except that the speed of the density waves should have the opposite signs, and that the mean particle velocity should decay with the volume fraction. As a last example, we point out that particles diffusiophoretically transported by a homogeneous solute gradient [24] should also display a very similar propagative dynamics, as they also induce a weak far field disturbance that has a dipolar symmetry [25]. This last example makes it clear that confinement is not a requirement to observe the propagation of dispersive waves. The model microfluidic experiment that we characterized and described in a quantitative fashion should be seen as a proxy to probe generic collective effects in particle-laden fluids driven out of equilibrium.

We acknowledge stimulating interactions with C. Savoie and M. Guérard. We thank D. Saintillan and T. Beatus for valuable comments and discussions, and Bertrand Levaché for help with the experiments. We also acknowledge funding from the National Science Foundation (Grant No. CBET-0746285 to E. L.)

[1] E. Guazzelli and J. Hinch, Annu. Rev. Fluid Mech. **43**, 97 (2011).
[2] S. Ramaswamy, Adv. Phys. **50**, 297 (2001).
[3] E. Evans and E. Sackmann, J. Fluid Mech. **194**, 553 (1988).
[4] B. X. Cui, H. Diamant, B. H. Lin, and S. A. Rice, Phys. Rev. Lett. **92**, 258301 (2004).
[5] J. Blawzdziewicz and E. Wajnryb, Phys. Fluids **20**, 093303 (2008).
[6] R. Di Leonardo, E. Cammarota, G. Bolognesi, H. Schafer, and M. Steinhart, Phys. Rev. Lett. **107**, 044501 (2011).
[7] J.-P. Hulin, A.-M. Cazabat, E. Guyon, and F. Carmona, *Hydrodynamics of Dispersed Media* (Elsevier, New York, 1990).
[8] R. D. Deegan, O. Bakajin, T. F. Dupont, G. Huber, S. R. Nagel, and T. A. Witten, Nature (London) **389**, 827 (1997).
[9] R. D. Deegan, O. Bakajin, T. F. Dupont, G. Huber, S. R. Nagel, and T. A. Witten, Phys. Rev. E **62**, 756 (2000).
[10] R. Seemann, M. Brinkmann, T. Pfohl, and S. Herminghaus, Rep. Prog. Phys. **75**, 016601 (2012).
[11] T. Beatus, R. Bar-Ziv, and T. Tlusty, Phys. Rep. **516**, 103 (2012).
[12] A. S. Popel and P. C. Johnson, Annu. Rev. Fluid Mech. **37**, 43 (2005).
[13] H. P. Zhang, A. Beer, E.-L. Florin, and H. L. Swinney, Proc. Natl. Acad. Sci. U.S.A. **107**, 13 626 (2010).
[14] R. Zhang, L. Turner, and H. C. Berg, Proc. Natl. Acad. Sci. U.S.A. **107**, 288 (2010).
[15] T. Beatus, T. Tlusty, and R. Bar-Ziv, Phys. Rev. Lett. **103**, 114502 (2009).
[16] T. Beatus, T. Tlusty, and R. Bar-Ziv, Nat. Phys. **2**, 743 (2006).
[17] F. Rouyer, D. Lhuillier, J. Martin, and D. Salin, Phys. Fluids **12**, 958 (2000).
[18] N. Champagne, R. Vasseur, A. Montourcy, and D. Bartolo, Phys. Rev. Lett. **105**, 044502 (2010).
[19] S. Thutupalli, R. Seemann, and S. Herminghaus, New J. Phys. **13**, 073021 (2011).
[20] See Supplemental Material at http://link.aps.org/supplemental/10.1103/PhysRevLett.111.118301 for more details about the experiments and the data analysis.
[21] See Supplemental Material at http://link.aps.org/supplemental/10.1103/PhysRevLett.111.118301 for a typical movie of a flowing microfluidic emulsion.
[22] H. Risken, *The Fokker-Planck Equation: Methods of Solution and Applications* (Springer-Verlag, Berlin, 1996).
[23] A. M. Menzel, Phys. Rev. E **85**, 021912 (2012).
[24] J. Palacci, C. Cottin-Bizonne, C. Ybert, and L. Bocquet, Soft Matter **8**, 980 (2012).
[25] J. L. Anderson, Annu. Rev. Fluid Mech. **21**, 61 (1989).